

Adaptive floating node method for modelling cohesive fracture of composite materials

Lu, X.; Chen, B. Y.; Tan, V. B.C.; Tay, T. E.

DOI

[10.1016/j.engfracmech.2018.03.011](https://doi.org/10.1016/j.engfracmech.2018.03.011)

Publication date

2018

Document Version

Final published version

Published in

Engineering Fracture Mechanics

Citation (APA)

Lu, X., Chen, B. Y., Tan, V. B. C., & Tay, T. E. (2018). Adaptive floating node method for modelling cohesive fracture of composite materials. *Engineering Fracture Mechanics*, 194, 240-261. <https://doi.org/10.1016/j.engfracmech.2018.03.011>

Important note

To cite this publication, please use the final published version (if applicable). Please check the document version above.

Copyright

Other than for strictly personal use, it is not permitted to download, forward or distribute the text or part of it, without the consent of the author(s) and/or copyright holder(s), unless the work is under an open content license such as Creative Commons.

Takedown policy

Please contact us and provide details if you believe this document breaches copyrights. We will remove access to the work immediately and investigate your claim.

Green Open Access added to TU Delft Institutional Repository

'You share, we take care!' - Taverne project

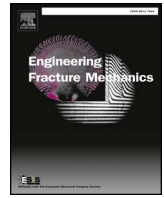
<https://www.openaccess.nl/en/you-share-we-take-care>

Otherwise as indicated in the copyright section: the publisher is the copyright holder of this work and the author uses the Dutch legislation to make this work public.



Contents lists available at ScienceDirect

Engineering Fracture Mechanics

journal homepage: www.elsevier.com/locate/engfracmech

Adaptive floating node method for modelling cohesive fracture of composite materials

X. Lu^{a,*}, B.Y. Chen^b, V.B.C. Tan^a, T.E. Tay^a^a Department of Mechanical Engineering, National University of Singapore, 117576, Singapore^b Faculty of Aerospace Engineering, Delft University of Technology, 2629HS Delft, Netherlands

ARTICLE INFO

Keywords:

- A. Adaptive modelling
- B. Fracture
- C. Finite element method
- D. Floating node method

ABSTRACT

The cohesive element has been widely employed to model delamination and matrix cracking in composite materials. However, an extremely fine mesh along the potential crack path is required to achieve accurate predictions of stresses within the cohesive zone. A sufficient number of cohesive elements must be present within the cohesive zone ahead of the crack tip, resulting in very high computational cost and time for application to practical composite structures. To mitigate this problem, an adaptive floating node method (A-FNM) with potential to reduce model size and computational effort is proposed. An element with adaptive partitioning capabilities is designed such that it can be formulated as a master element, a refined element and a coarsened element, depending on the damage state in the progressive damage process. A relatively coarse overall mesh may be used initially, and by transforming the element configurations adaptively, the local refinement and coarsening schemes are applied in the analysis. The localized stress gradient ahead of the crack front within the refinement zone is captured by the refined elements. The refinement and coarsening operations are performed at the elemental level with fixed nodal connectivity, so that global successive remeshing in adaptive mesh refinement (AMR) techniques is avoided; this is the key difference between AMR and A-FNM. It is demonstrated that, without loss of accuracy, the present method simplifies the modelling procedure and reduces computational cost.

1. Introduction

Delamination and matrix cracking are two of the most common failure mechanisms for laminated composite materials arising from low-velocity impacts, bearing loads or manufacturing defects. Their interaction and propagation significantly affect the strength and integrity of composite structures [1].

Two explicit approaches are commonly adopted to model fracture in composite materials: the virtual crack closure technique (VCCT) [2,3] and cohesive zone model (CZM) [4,5]. Assuming self-similar crack propagation, VCCT may be performed to calculate the strain energy release rate and predict crack propagation. It has been applied to model delamination migration in composite laminates [6] with an accompanying failure criterion for matrix crack initiation. In general, however, the assumption of an initial crack and requirement for successive remeshing operations make the application of this method rather cumbersome. The other alternative, the cohesive element (CE) method, is formulated based on the CZM and has been widely used to model the onset and propagation of cohesive cracks [7–15]. A cohesive zone (or fracture process zone) is introduced in front of the crack tip to model the material damaging mechanisms. Combined with other numerical methods such as the extended finite element method (XFEM) and

* Corresponding author.

E-mail address: xinlu@u.nus.edu (X. Lu).

Nomenclature		ε	strain
\mathcal{A}	assembly operator	σ	stress
\mathbf{D}	constitutive matrix	A-FNM	adaptive floating node method
e	relative error	AMR	adaptive mesh refinement
\mathbf{K}	stiffness matrix	B-K	Benzeggagh–Kenane
l_{ch}	characteristic length	CE	cohesive element
l_{CE}	length of cohesive element	CZM	cohesive zone model
l_{CZ}	length of cohesive zone	DCB	double cantilever beam
l_{rf}	length of refinement zone	DoF	degree of freedom
\mathbf{N}	shape function matrix	DM	delamination migration
\mathbf{Q}	nodal force vector	ENF	end notch flexure
\mathbf{t}	traction	FE	finite element
\mathbf{u}	displacement	FNM	floating node method
U	strain energy	MMB	mixed-mode bending
δ	variation operator	OHT	open-hole tension
Δ	separation	SE	solid element
ζ	tolerance	VCCT	virtual crack closure technique
		XFEM	extended finite element method

floating node method (FNM) [16–25], modified or enhanced CEs have been used to predict the coupled interaction between matrix cracking and delamination propagation.

However, to achieve accurate predictions with the CZM, sufficient number of CEs must be used within the moving cohesive zone ahead of the crack front, which is extremely small compared with the scale of most structures [26,27]. It has been found that significant mesh dependency and over-prediction of structural strength can be expected if coarse CE meshes are adopted in the simulations [12]. Consequently, application of the CE modelling requires an excessively refined mesh (usually determined by the cohesive zone length) along the potential crack path, leading to very high computational expense.

To address the strict mesh size requirement, which is the significant drawback of CE modelling, several numerical techniques have been proposed. Guimatsia et al. enriched the CE with analytical solutions obtained from the beam on an elastic foundation and hence increased the size requirement in the simulation [28–30]. Turon et al. introduced an engineering solution: by artificially reducing interface strength, CE models with relatively coarse meshes may provide satisfactory results [12]. On the other hand, globally fine meshes can be avoided by employing adaptive mesh refinement (AMR) techniques [31–33]. The meshes ahead of the crack tip were refined to the required length scale while, in the far field, relatively coarse meshes could be used [34–38]. To reduce the number of CEs in the model, Shor et al. adaptively inserted and deleted the CEs around the crack tip region during delamination propagation [39]. Other adaptive modelling techniques and enriched formulations have been researched in the literature [40–44]. Although these techniques may, to some extent, overcome the difficulties of CE modelling, there are also significant limitations. For instance, if reduced interface strength is used, the cohesive traction fields in front of the crack tip could not be faithfully captured and user experience is needed to choose the appropriate mesh size and the corresponding reduced strength parameters. AMR techniques generally require continuing global mesh regeneration and the associated nodal mapping, which in turn increases overall computational cost and implementation complexity.

Within the very small cohesive zone, it is necessary for the mesh to be very fine; however, in the intact and the extensively failed regions, there is no need for such refinement. Based on this understanding, an efficient adaptive floating node method (A-FNM) is developed in this study. The floating node method (FNM) is a recently developed discrete crack method for modelling progressive failure of fiber-reinforced composites [19–21]. In the FNM, besides the standard element nodes, additional floating nodes are included in the formulation to potentially capture discontinuities introduced by the cracks. The performance and accuracy of the FNM have been validated in previous work [19–21]. Based on the same framework, the A-FNM is proposed and an adaptive element is formulated, which may be interchangeably partitioned into one of three configurations (namely, the master element, refined element and coarsened element), depending on the stage of damage evolution experienced by the element. The master and coarsened elements are used in fields far from the critical damaged region while the refined elements are assigned ahead of the crack tip. By altering the element configurations adaptively in the analysis, local refinement and coarsening are achieved within an originally coarse mesh. The refined region moves together with the propagating crack front, more accurately modelling the progressive damage process. This would be particularly useful in cases of advancing delamination or concentrated damage fronts.

Although the presented A-FNM shares some features in common to the AMR, several drawbacks of AMR have been overcome:

- Global successive remeshing is not required: the refinement and coarsening operations in A-FNM are performed on the elemental level. By simply transforming the element configurations, local refinement and coarsening with fixed nodal connectivity is achieved.
- Mapping of nodal information is not required: all the nodal information, e.g., the displacements and the failure indices, is stored in the same element throughout the simulation. Mapping information between different meshes is avoided.
- Specially-designed solvers are not required: the proposed A-FNM can be generally implemented as a user-defined element in commercial finite element (FE) software packages such as Abaqus.

As a demonstration in this paper, the proposed A-FNM is applied to the modelling of delamination and matrix cracking in composite materials. In Section 2, a brief review on CZM and the associated cohesive zone length is presented. The details of A-FNM and the corresponding refinement and coarsening schemes are described in Section 3. Section 4 provides the FE formulation and implementation details. Several verification examples are given in Section 5. Finally, some conclusions are drawn in Section 6.

2. The cohesive zone model and cohesive zone length

In the present work, the A-FNM is formulated based on the mesh size requirement of the CE, guided by the cohesive zone length in CZM. In this section, we briefly review the theory of CZM and introduce the cohesive zone length in numerical simulations.

As shown in Fig. 1a, the CZM developed by Dugdale [4] and Barenblatt [5] introduced a fracture process zone (or cohesive zone) in front of the crack tip, and a cohesive law was adopted to describe the traction-separation behaviors of the crack surfaces [45]. Considering the bilinear cohesive law shown in Fig. 1a, the material strength is characterized by the maximum traction t_{nc} , beyond which a softening curve is used to represent the irreversible behavior of the damaged material. The area under the traction-separation curve is equal to the fracture toughness of the material.

Based on the CZM, a characteristic length, l_{ch} , is proposed to estimate the size of the cohesive zone [46–48]. For fracture analysis of orthotropic materials (e.g., composite materials) in an infinite domain, the characteristic lengths for mode I and mode II loading are given by:

$$l_{ch,I} = \frac{E'_I G_{IC}}{(\sigma_{I,max})^2} \tag{1}$$

$$l_{ch,II} = \frac{E'_{II} G_{IIC}}{(\sigma_{II,max})^2} \tag{2}$$

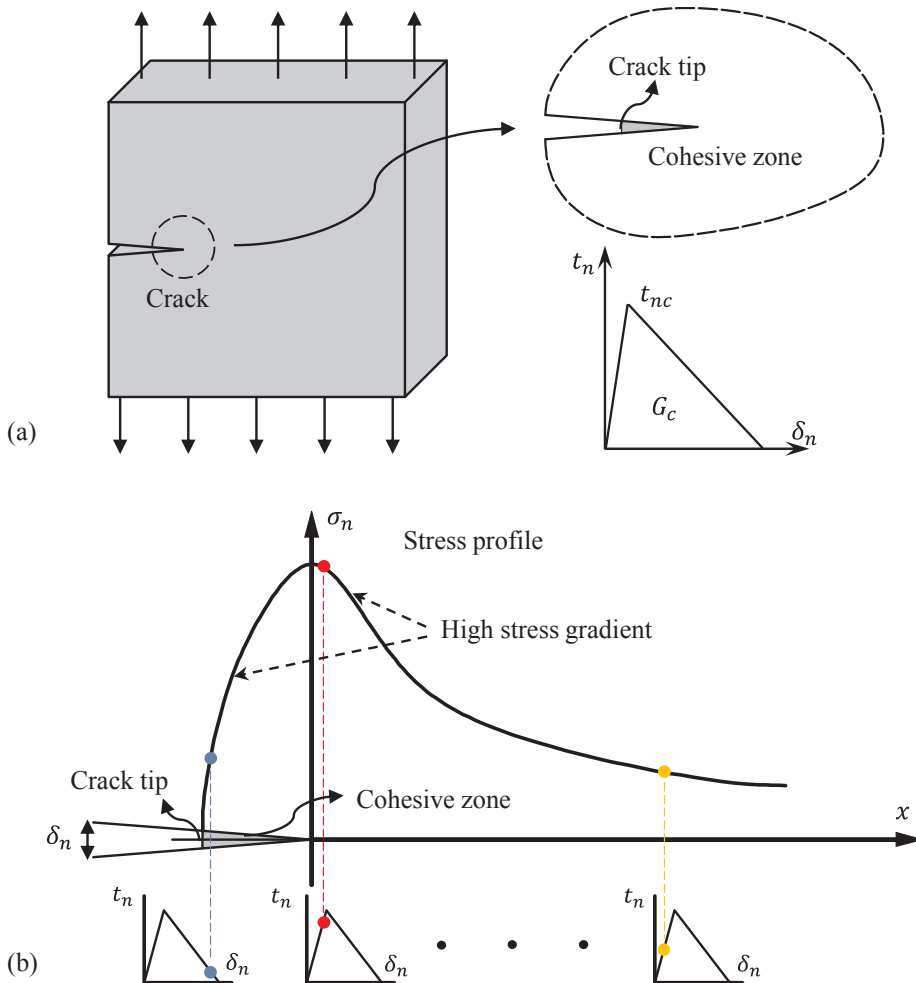


Fig. 1. (a) Cohesive zone model and the bilinear traction-separation cohesive law; (b) a typical stress profile ahead of the crack tip.

where G_{IC} and G_{IIC} are the mode I and mode II fracture toughness; $\sigma_{I,max}$ and $\sigma_{II,max}$ are the strength of two modes, respectively. E'_I and E'_{II} are the equivalent elastic moduli, depending on the material properties and loading conditions (details can be found in [26,49–51]). For slender laminates, Eq. (1), (2) can be further modified as [26,52]:

$$l_{ch,I}^s = (l_{ch,I})^{1/4} h^{3/4} \tag{3}$$

$$l_{ch,II}^s = \sqrt{(l_{ch,II})} h \tag{4}$$

where h is the half-thickness of the laminate.

It was reported that the characteristic length is within an order of magnitude of the cohesive zone length [51] and may be used to estimate the cohesive zone length (l_{CZ}) [26,27]:

$$l_{CZ} = 0.5[\min(\text{Eq. (1), (2), (3), (4)})] \tag{5}$$

As can be seen from stress profile shown in Fig. 1b, the cohesive law falls into the softening part ahead of the crack tip, which represents material degradation in the cohesive zone. The stress increases initially from zero to the material strength, and high stress gradient is expected. It has been demonstrated that for accurate failure predictions, at least two or three CEs should be used to model the cohesive zone [12,53]. In this paper, the number of CEs used in this critical region is three, so that the length of CE, l_{CE} , is calculated as:

$$l_{CE} = \frac{l_{CZ}}{3} \tag{6}$$

Eq. (6) provides an *a priori* size requirement for CE in the A-FNM formulation in Section 3.

3. Adaptive floating node method (A-FNM)

In this section, a detailed formulation of the A-FNM and the corresponding refinement and coarsening schemes are presented. In the present work, we focus on cohesive fracture problems and propose an efficient numerical approach that addresses the excessive mesh size requirement in conventional application of CEs. Based on the FNM [19], an enriched element with adaptive partitioning capabilities is developed. Several configurations of the element are illustrated, together with the corresponding automatic refinement and coarsening algorithm.

3.1. Adaptive floating node element

As shown in Fig. 2, the adaptive element is defined by real and floating nodes with the associated degrees of freedom (DoF) [19–21]. First, as usual the real nodes are used to construct the elements and discretize the domain of the solid body. Each element is further enriched with pre-allocated floating nodes in anticipation of possible partitioning of the element. The corresponding nodal

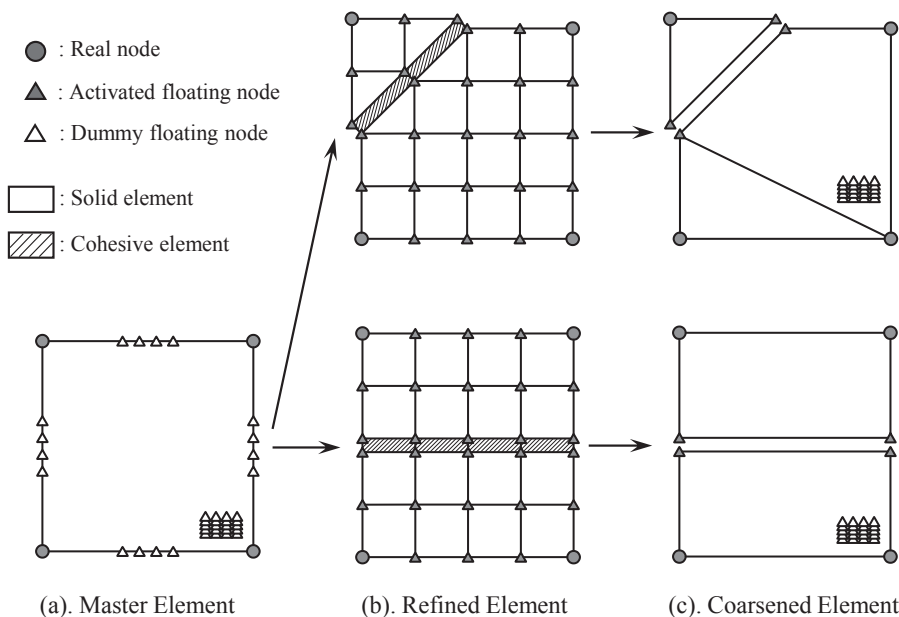


Fig. 2. Adaptive floating node element with partitioning capabilities: (a) master element configuration; (b) refined element configuration; (c) coarsened element configuration.

connectivity of real and floating nodes are established within the element. At this stage, it is not necessary to define the position vectors of the floating nodes and they can be simply assigned to the origin of the coordinate system (zero position vectors).

While the real nodes are used to construct the original model, the floating nodes are successively deployed in subsequent steps of the analysis to refine the element and model the discontinuities due to cracking as determined by failure initiation and fracture criteria (Fig. 2b and c). In Fig. 2a, some floating nodes are assigned to the edges and shared by the adjacent elements. This arrangement ensures continuation of crack propagation across element boundaries. The rest of the floating nodes are reserved for deployment within the element.

Each floating node may assume one of two states: dummy or active. A dummy floating node has no stiffness or force is associated with its DoF but is activated when partitioning the parent element into sub-elements (Fig. 2b and c). The coordinates of the node are calculated based on the configuration of the partition. The DoFs of the newly activated floating node are included in the global equilibrium equation.

For application to fracture, three element configurations are possible: the master element, refined element and coarsened element. Only real nodes are used in the master element, while all floating nodes remain as dummy nodes (i.e. undeployed), with the usual stiffness matrix of a standard quadrilateral element:

$$\mathbf{K}_{master} = \mathbf{K}_{quad} \tag{7}$$

However, when an element is approached by an advancing crack front, it is transformed to the refined configuration (Fig. 2b). CEs are inserted into the element for predicting the propagation of the crack. The dummy floating nodes within the element are activated to refine each of the sub solid elements (SEs) and sub-CEs to a size smaller than the required length scale (Eq. (6)). Thus, the stiffness matrix of the refined element is simply an assembly of the stiffnesses of all sub-elements within:

$$\mathbf{K}_{refined} = \mathcal{A}(\mathbf{K}_s^i, \mathbf{K}_c^j), \quad i = 1, 2, \dots, N_s, \quad j = 1, 2, \dots, N_c \tag{8}$$

where \mathcal{A} is the assembly operator; \mathbf{K}_s^i and \mathbf{K}_c^j denote the stiffness matrices of the i^{th} SE and j^{th} CE; N_s is the number of sub-SEs and N_c is the number of sub-CEs, respectively. In this way, crack propagation may be modelled by failing the sub-CEs.

Once the crack tip and the associated cohesive zone has passed the refined elements, the high stress gradients no longer exist in these elements. The refined element is re-coarsened and the sub-CEs are deleted. The floating nodes on the cracked edges remain active to describe the crack surfaces, while the remaining floating nodes and their corresponding DoFs are deactivated and removed from the overall element formulation. Therefore, the stiffness matrix of a coarsened element is given by:

$$\mathbf{K}_{coarsened} = \mathcal{A}(\mathbf{K}_s^i), \quad i = 1, 2, \dots, N_s \tag{9}$$

The element introduced here possesses adaptive partitioning capabilities, i.e., it can be readily converted to any pre-defined configuration at any stage of the FE analysis. Since the nodes as well as the connectivity are predefined before the analysis, global remeshing and stop-restart operations are not required. Details of the A-FNM are presented in the following subsections.

3.2. Formulation of the refined element configuration

In the proposed A-FNM scheme, the element is first converted into a refined configuration to model the progressive fracture process. Assuming the initial mesh yields a converged solution for linear elastic analysis and that the size requirement in Eq. (6) is satisfied, the refined element configuration can be determined. Assuming the element size of the initial mesh is l_0 and the required size of CE is l_{CE} , the number of sub-CEs embedded in refined configuration can be calculated as:

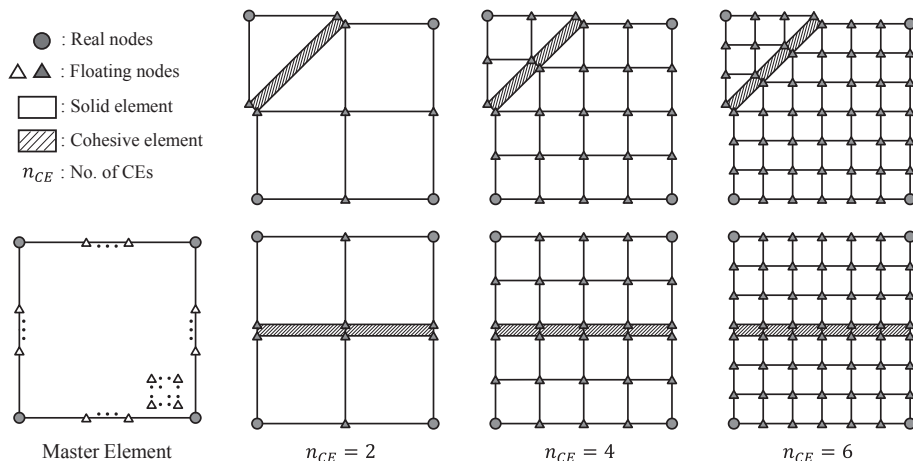


Fig. 3. Refined element configurations with different n_{CE} .

$$n_{CE} = \left\lceil \frac{l_0}{l_{CE}} \right\rceil \tag{10}$$

where $\lceil \cdot \rceil$ is the ceiling function which returns the smallest integer larger than the input value. n_{CE} as given by Eq. (10) determines the total number of floating nodes that should be predefined in the element as well as the configuration of the refined element (Fig. 3). For practical implementation, the number of sub-CEs is reduced by half if the crack propagates across the neighboring edges of the master element. It is worth noting that the A-FNM proposed in the present work possesses adaptivity and flexibility, i.e., the associated refined configurations can be tailored automatically for a given n_{CE} .

3.3. Refinement zone and refinement schemes

In conventional AMR techniques, the mesh refinement operations are generally applied with *a posteriori* error estimators [31,32]. If the errors based on current mesh exceed the prescribed tolerance, remeshing will be performed and the size of the refined mesh can be estimated by the predicted errors. Automatic mesh generators repeat this process of successive refinement. In the proposed A-FNM, however, an *a priori* refinement criterion for CE simulation can be established based on the theory of CZM as introduced in Section 2.

As shown in Fig. 1b, the stress gradient remains very high for the region within and right after the cohesive zone, and to correctly capture the material behaviors in that region, refined elements should be employed. For this reason, a refinement zone ahead of the crack tip is defined, and all the elements within this zone should be formulated as refined configurations (Fig. 4). This refinement zone is attached to the moving crack front during the progressive damage process (Fig. 4b and c). In general, the refinement zone should be larger than the cohesive zone. Based on previous studies on crack tip traction profiles [12,26–28], the length of the refinement zone (l_{rf}) may be set as three times the cohesive zone length, i.e.:

$$l_{rf} = 3l_{CZ} \tag{11}$$

The refinement zone and the associated refinement scheme is illustrated through an example shown in Fig. 4. As introduced in Section 3.1, the initial model is built up by the real nodes and the dummy floating nodes predefined in the element (Fig. 4a). The global nodal connectivity is given by:

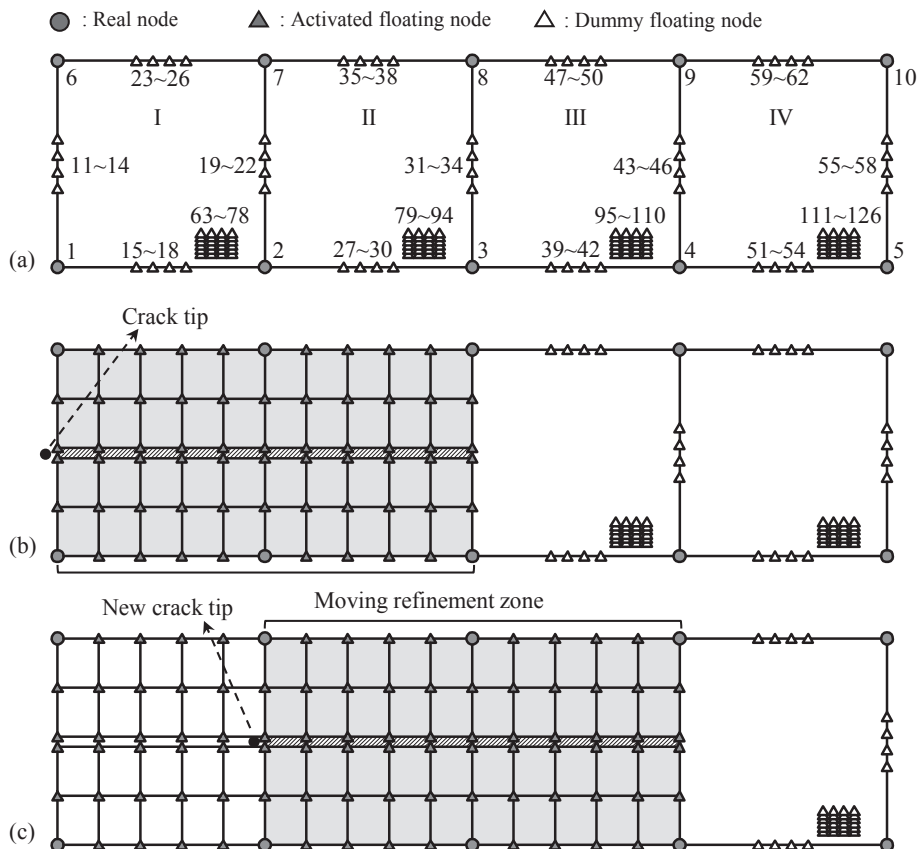


Fig. 4. Element refinement schemes with moving refinement zone: (a) initial configuration and global connectivity; (b) refined elements in the refinement zone; (c) moving refinement zone along with the crack propagation.

$$\begin{aligned}
 \text{I: } & \{1,2,7,6,11 \sim 14,15 \sim 18,19 \sim 22,23 \sim 26,63 \sim 78\} \\
 \text{II: } & \{2,3,8,7,19 \sim 22,27 \sim 30,31 \sim 34,35 \sim 38,79 \sim 94\} \\
 \text{III: } & \{3,4,9,8,31 \sim 34,39 \sim 42,43 \sim 46,47 \sim 50,95 \sim 110\} \\
 \text{IV: } & \{4,5,10,9,43 \sim 46,51 \sim 54,55 \sim 58,59 \sim 62,111 \sim 126\}
 \end{aligned} \tag{12}$$

The number of the embedded floating nodes and the corresponding refined configurations are determined by n_{CE} , which can be evaluated from the material properties and the loading conditions (Eq. (10)). Here, n_{CE} is set to 5 in the example (Fig. 4).

As shown in Fig. 4a, far away from the crack front, the initial intact material is modelled by master elements, and the dummy floating nodes in elements I–IV are not used in this step. Hence, only nodes 1–10 are engaged in the global calculation. When the crack approaches element I during the damage process (Fig. 4b), elements I and II enter the refinement zone. The dummy floating nodes in elements I and II are activated and they are converted to the refined configurations. Further loading causes progressive failure of the sub-CEs while the crack advances in element I. Subsequently, element III enters the refinement zone and is refined as well (Fig. 4c). In this way, adaptive refinement is performed while keeping the overall nodal connectivity the same as given in Eq. (12); hence no updating is required.

Discussions on the effects of refinement zone length on numerical predictions are provided in Section 5 via some examples.

3.4. Element coarsening schemes

Based on a *a posteriori* error control criterion on the strain energy, the element coarsening schemes for A-FNM are introduced in this subsection. As shown in Fig. 5a, with the increase of the external load, all the sub-CEs in the refined element may be failed and the material behaviors are fully governed by the linear SEs 1–20. However, the size of sub-SEs in a refined configuration may be unnecessarily small for the purpose of modelling elastic deformation. Therefore, the following element coarsening procedure is proposed to reduce model size and computational cost.

The strain energy for the refined element with failed interface is calculated as (Fig. 5a):

$$U_{ref} = \sum_i \int \sigma_i: \varepsilon_i dV_i, \quad i = 1,2,\dots,20 \tag{13}$$

where σ_i and ε_i are the stress and strain tensor for the sub-SE i in the refined element and V_i is the corresponding volume. Firstly, assume that the refined element is completely coarsened (Fig. 5b) and the strain energy for this coarsened configuration is given as:

$$U_{crs} = \sum_i \int \sigma_i: \varepsilon_i dV_i, \quad i = 1,2 \tag{14}$$

Then, the change in strain energy induced by coarsening the element is evaluated:

$$e = \frac{|U_{ref} - U_{crs}|}{U_{ref}} \times 100\% \tag{15}$$

A tolerance ζ is prescribed and the coarsening operation is applied, if the error calculated from Eq. (15) is within the tolerance, i.e., the coarsening criterion is satisfied:

$$e \leq \zeta \tag{16}$$

Otherwise, if Eq. (16) is not satisfied, an intermediate configuration (Fig. 5c) is considered, and a smaller sub-SE size is adopted. The previous procedures (Eqs. (14) and (15)) are repeated until the coarsening criterion Eq. (16) is met by deactivating the

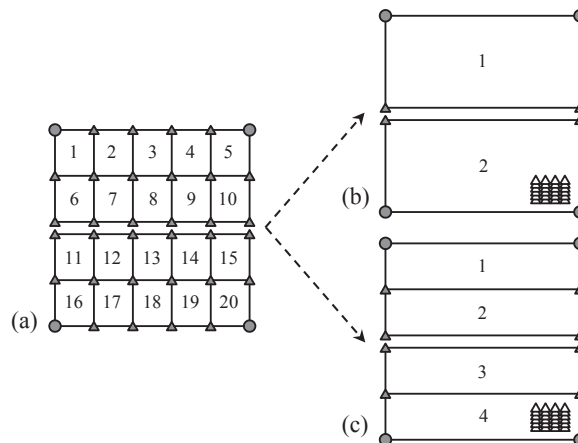


Fig. 5. Element coarsening schemes: (a) refined element with failed sub-CEs; (b) completely coarsened element configuration; (c) partially coarsened element configuration.

appropriate number of floating nodes.

4. Implementation details

In this section, implementation of the A-FNM in FE analysis is described. The general FE formulation including the CZM is presented. We also introduce the numerical techniques that can deal with the compatibility problems arising from the proposed A-FNM.

4.1. Finite element formulation

Quasi-static fracture problem with cohesive zone modelling is considered in FE analysis. In the absence of body forces, the weak form of governing equation is obtained from principle of virtual work:

$$\int_{\Omega} \delta \varepsilon : \sigma dV + \int_{\Gamma_{coh}} \delta \Delta \cdot \mathbf{t}_{coh} d\Gamma_{coh} = \int_{\Gamma_t} \delta \mathbf{u} \cdot \mathbf{t} d\Gamma_t \tag{17}$$

where \mathbf{u} is the solution of displacement field and Δ is the separation between the cohesive crack surfaces. Furthermore, ε and σ are strain and stress tensors, related by a constitutive tensor \mathbf{D} , $\sigma = \mathbf{D} : \varepsilon$; \mathbf{t} and \mathbf{t}_{coh} are the traction vectors acting the on the force boundary Γ_t and cohesive boundary Γ_{coh} , respectively.

In FE analysis, the domain is discretized into SEs and CE to represent bulk solids and interfaces respectively. The element displacement fields are given by:

$$\mathbf{u} = \mathbf{N}_s \mathbf{u}_n \tag{18}$$

$$\Delta = \mathbf{N}_c \mathbf{u}_n \tag{19}$$

where \mathbf{N}_s and \mathbf{N}_c are the shape function matrices for SE and CE, respectively. \mathbf{u}_n is the nodal displacement vector of the elements.

The strains are related to the displacements by the strain-displacement transformation matrix \mathbf{B} ,

$$\varepsilon = \mathbf{B} \mathbf{u}_n \tag{20}$$

The stresses and cohesive tractions are given in terms of the nodal displacements through the constitutive relations:

$$\sigma = \mathbf{D} \varepsilon = \mathbf{D} \mathbf{B} \mathbf{u}_n \tag{21}$$

$$\mathbf{t}_{coh} = \mathbf{D}_c \Delta = \mathbf{D}_c \mathbf{N}_c \mathbf{u}_n \tag{22}$$

where \mathbf{D}_c is the constitutive matrix for CEs. Substituting Eqs.(18)–(22) into Eq. (17), the governing equation becomes:

$$\int_{\Omega} \delta \mathbf{u}_n' \mathbf{B}' \mathbf{D} \mathbf{B} \mathbf{u}_n dV + \int_{\Gamma_{coh}} \delta \mathbf{u}_n' \mathbf{N}_c' \mathbf{D}_c \mathbf{N}_c \mathbf{u}_n d\Gamma_{coh} = \int_{\Gamma_t} \delta \mathbf{u}_n' \mathbf{N}_s' \mathbf{t} d\Gamma_t \tag{23}$$

$$\left(\int_{\Omega} \mathbf{B}' \mathbf{D} \mathbf{B} dV + \int_{\Gamma_{coh}} \mathbf{N}_c' \mathbf{D}_c \mathbf{N}_c d\Gamma_{coh} \right) \mathbf{u}_n = \int_{\Gamma_t} \mathbf{N}_s' \mathbf{t} d\Gamma_t \tag{24}$$

Let \mathbf{K}_s^i and \mathbf{K}_c^j denote the stiffness matrices of i^{th} SE and j^{th} CE, respectively; let \mathbf{Q}_s^i denote the external force vector applied on i^{th} SE. Then Eq. (24) can be rewritten as:

$$\mathcal{A}(\mathbf{K}_s^i, \mathbf{K}_c^j) \mathbf{u}_n = \mathcal{A}(\mathbf{Q}_s^i), \quad i = 1, 2, \dots, N_s, \quad j = 1, 2, \dots, N_c \tag{25}$$

where \mathcal{A} is the assembly operator; N_s and N_c are the total numbers of SEs and CEs in the model, respectively. Eq. (25) finally leads to:

$$\mathbf{K} \mathbf{u}_n = \mathbf{Q} \tag{26}$$

with $\mathbf{K} = \mathcal{A}(\mathbf{K}_s^i, \mathbf{K}_c^j)$ and $\mathbf{Q} = \mathcal{A}(\mathbf{Q}_s^i)$, respectively.

4.2. Constitutive relation of cohesive zone model (CZM)

A mixed-mode bilinear cohesive law is adopted to construct the CE (Fig. 6):

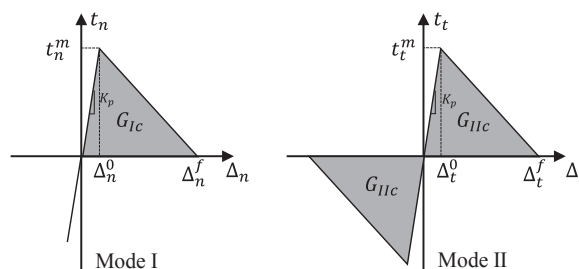


Fig. 6. Cohesive law for mode I and mode II fracture.

$$\int_0^{\Delta_e^f} t_e d\Delta_e = \frac{1}{2} t_e^m \Delta_e^f = G_{mc} \tag{27}$$

where superscript *f* represents final failure and *m* represents maximum value; variable with subscript *e* is the effective value for mixed-mode failure:

$$\Delta_e = \begin{cases} \sqrt{\Delta_n^2 + \Delta_t^2} & \Delta_n \geq 0 \\ \Delta_t & \Delta_n < 0 \end{cases}, \quad t_e = \begin{cases} (t_n \Delta_n + t_t \Delta_t) / \Delta_e & \Delta_n \geq 0 \\ t_t & \Delta_n < 0 \end{cases} \tag{28}$$

where Δ_n and Δ_t are the normal and transverse separations; t_n and t_t are the corresponding tractions, calculated as:

$$t_n = (1-d_m)K_p \Delta_n, \quad t_t = (1-d_m)K_p \Delta_t \tag{29}$$

where K_p is the penalty stiffness and d_m is the damage variable obtained from the cohesive law.

The Benzeggagh–Kenane (B-K) law is adopted for the mixed-mode energy release rate [54]:

$$G_{mc} = G_{Ic} + (G_{IIc} - G_{Ic}) \left(\frac{G_{II}}{G_I + G_{II}} \right)^\eta \tag{30}$$

where G_{Ic} and G_{IIc} are the fracture toughness for mode I and mode II failure; η is the material properties obtained from experimental tests; G_I and G_{II} are determined at the failure onset as:

$$G_I = \max(0, \Delta_n) \cdot t_n, \quad G_{II} = \Delta_t t_t \tag{31}$$

4.3. Master-Slave constraint

To ensure the compatibility between different element configurations, the master-slave constraints are applied on the transitional edges. As shown in Fig. 7, the floating nodes on the edges that connect the refined and master elements are set as the slave nodes, while the corresponding real nodes at the endpoints are set as the master nodes. In this way, the displacements of the slave nodes can be interpolated by the values of master nodes:

$$\begin{aligned} \mathbf{u}_i &= \frac{d_{i,5}}{d_{1,5}} \mathbf{u}_1 + \frac{d_{i,1}}{d_{1,5}} \mathbf{u}_5, \quad i = 2, 3, 4 \\ \mathbf{u}_i &= \frac{d_{i,10}}{d_{5,10}} \mathbf{u}_5 + \frac{d_{i,5}}{d_{5,10}} \mathbf{u}_{10}, \quad i = 6, 7, 8, 9 \end{aligned} \tag{32}$$

where d_{ij} is the distance between nodes *i* and *j*.

Applying the constraint equations in Eq. (32), the slave nodes and the associated DoFs are removed from the formulation of the stiffness matrix and the displacements of those constrained edges are fully characterized by the real end nodes. In this way, the compatibility problems brought about by A-FNM are properly addressed.

4.4. Crack propagation and element partitioning

The proposed A-FNM can be applied in unstructured meshes to model the crack propagation. Upon satisfaction of failure criterion, the initiation of new cracks is assumed at the center of the element (Fig. 8a). The crack angle α is determined from the fiber direction or the elemental state of stress, depending on the problems analyzed. On the other hand, for an existing crack propagating across an element, the crack path is determined by the fiber orientation or crack propagation criterion (Fig. 8b) and does not have to pass through the element center.

In implementation, the crack path may sometimes approach very close to a node (Fig. 8c). To avoid consequent sub-elements with very high aspect ratios, a small deviation of the crack path is imposed [20]. This deviation, δ_{dev} , is set to be 10% of the original edge length of the element (Fig. 8c).

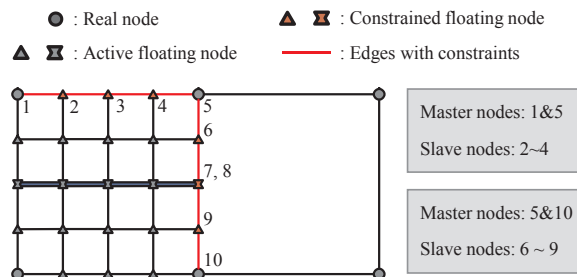


Fig. 7. Master slave constraints on transitional edges.

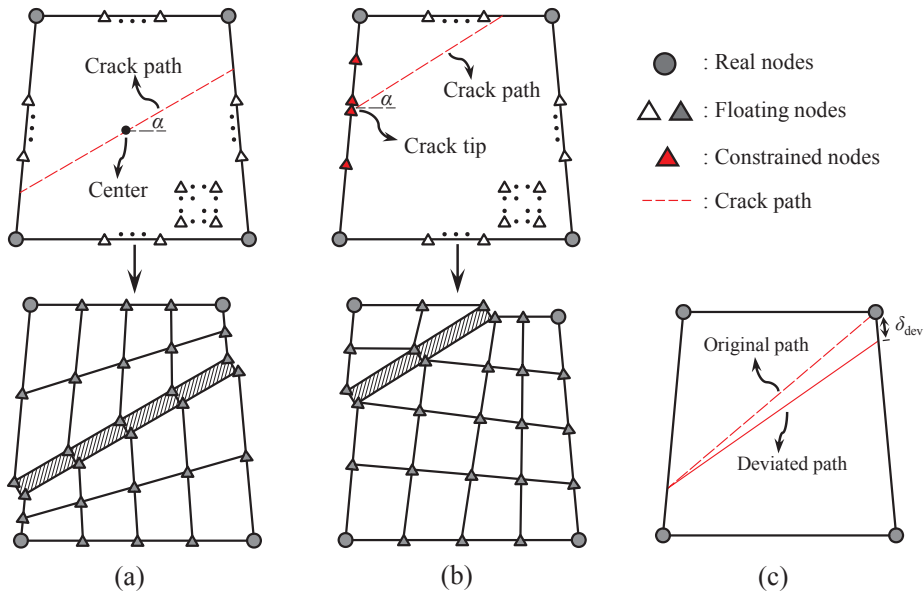


Fig. 8. The crack propagation and element partitioning: (a) crack initiates from the center of an element; (b) crack propagates across an element; (c) deviation of crack path around a node.

5. Numerical verification

In this section, a few benchmark problems are selected to demonstrate the accuracy and efficiency of the proposed A-FNM. The first is the double cantilever beam (DCB) test for mode I delamination propagation, followed by the end notch flexure (ENF) for mode II and the mixed-mode bending (MMB) test. Open-hole tension (OHT) of a composite laminate is then analyzed. Finally, the delamination migration (DM) in cross-ply laminates is modelled with A-FNM.

5.1. Double cantilever beam (DCB) test

A typical DCB [8] is shown in Fig. 9. The dimensions of the beam are length $2L = 100$ mm, thickness $h = 3$ mm and width 20 mm. An initial crack of length $a = 30$ mm is embedded in the beam and the material properties are given in Table 1. The delamination propagates under the prescribed displacements Δ at the loaded end of the beam.

5.1.1. Length of cohesive zone and refinement zone

The length of the cohesive zone for this problem, based on the material properties of Table 1 and Eq. (5), is calculated as:

$$l_{CZ} \approx 0.5836 \text{ mm} \tag{33}$$

Since three CEs are assigned in the cohesive zone to guarantee accurate predictions, the required size for CE is calculated as:

$$l_{CE} = \frac{l_{CZ}}{3} \approx 0.1945 \text{ mm} \tag{34}$$

In addition, the refinement zone is set to be three times the cohesive zone, therefore:

$$l_{rf} = 3l_{CZ} \approx 1.7508 \text{ mm} \tag{35}$$

Validation of Eqs. (33)–(35) is given through numerical analysis.

Fig. 10 shows a mesh sensitivity test for the CEs modelling the mode-I delamination fracture. With mesh size smaller than or equal to 0.2 mm (Eq. (34)), accurate and converged predictions are achieved when benchmarked with results from VCCT [8] and analytical [55] models. However, if coarse meshes are adopted (larger than 0.2 mm), incorrect results are obtained. As can be observed from the

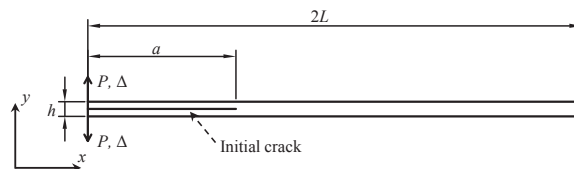


Fig. 9. DCB test: set-up and loading conditions.

Table 1
Material properties used in Section 5 [6,20,39].

	E_{11} (GPa)	E_{22}/E_{33} (GPa)	G_{12}/G_{13} (GPa)	G_{23} (GPa)	ν_{12}/ν_{13} (-)	G_{Ic} (N/mm)	G_{IIc} (N/mm)	σ_{max}/τ_{max} (Mpa)	η (-)
DCB	135.3	9	5.2	3.08	0.24	0.28	–	57	–
ENF	135.3	135.3	–	–	0.25	–	4	57	–
MMB	135.3	9	5.2	3.08	0.24	4	4	57	2
OHT	161	11.4	5.17	3.08	0.32	0.29	0.63	40/50	2
DM	161	11.38	5.17	3.98	0.32	0.21	0.77	60/90	2.1

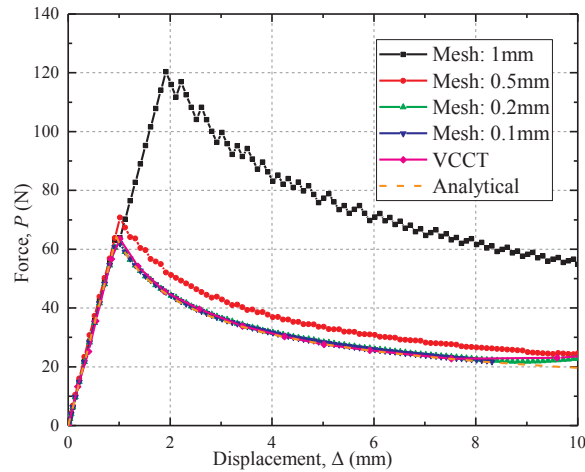


Fig. 10. Load-displacement curves for DCB test with different CE mesh sizes.

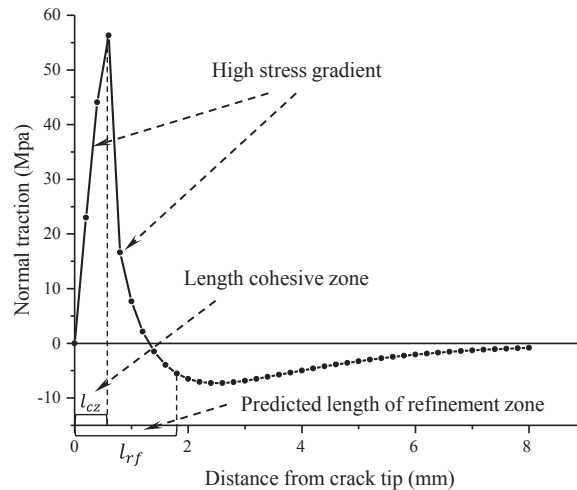


Fig. 11. Normal traction vs. the distance ahead of the crack tip: at the onset of delamination for model I DCB test.

loading curves, the strength of the structure is over-predicted by about 100% for the model with 1 mm mesh.

Fig. 11 shows the distribution of normal traction ahead of the crack tip for 0.2 mm size mesh. At the onset of the delamination, the cohesive zone length obtained from the numerical results is 0.6 mm, satisfying the criterion of Eq. (33). The estimated refinement zone length given by Eq. (35) is therefore adequate.

5.1.2. A-FNM modelling for DCB mode-I delamination

A-FNM is applied to simulate the DCB mode I delamination propagation. Based on the previous discussions, the refinement zone length is set to be 2 mm and the tolerance for coarsening schemes is prescribed as 5%, i.e.:

$$l_{rf} \equiv 2 \text{ mm} \tag{36}$$

$$\zeta \equiv 5\% \tag{37}$$

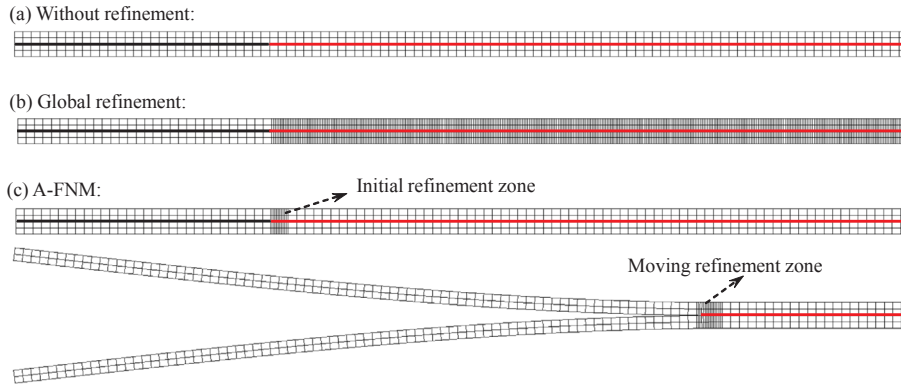


Fig. 12. Meshes for traditional FEM and A-FNM models: (a) FEM model without refinement (1mm mesh); (b) FEM model with global refinement (0.2 mm mesh); (c) A-FNM model with moving refinement.

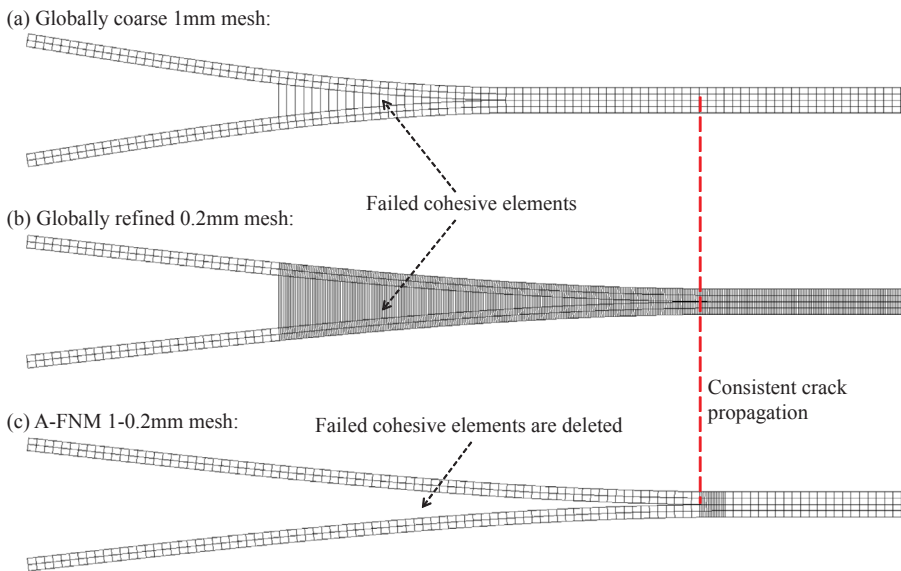


Fig. 13. Delamination evolution predicted by traditional FEM and A-FNM models: (a) uniform 1 mm coarse FEM mesh; (b) uniform 0.2 mm fine FEM mesh; (c) A-FNM 1–0.2 mm mesh with 2 mm refinement zone.

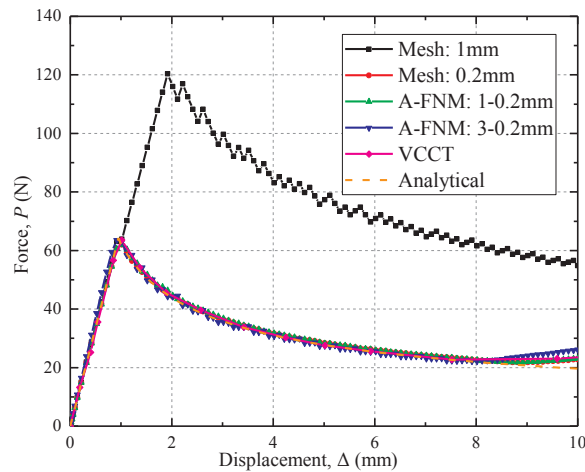


Fig. 14. Loading curves obtained from traditional FEM models and A-FNM models.

Table 2
DCB: computational cost for different models (CPU time, X5690@3.47 GHz).

Mesh size (mm)	1	0.2	A-FNM 1-0.2	A-FNM 3-0.2
Computational time (s)	110.8	640.58	368.82	336.71

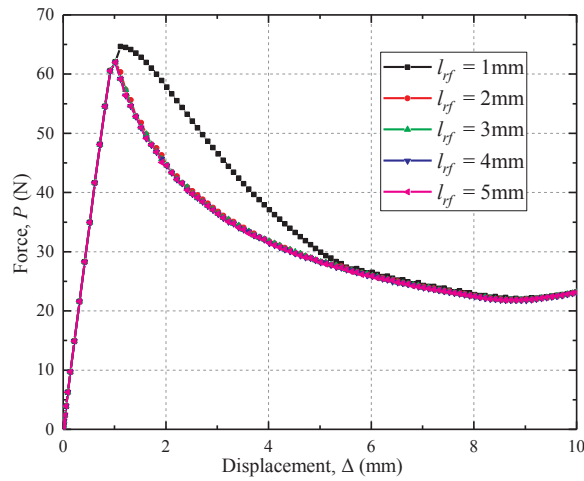


Fig. 15. DCB: Sensitivity to length of refinement zone.

Table 3
DCB: computational times for A-FNM with different l_{rf} (CPU time, X5690@3.47 GHz).

l_{rf} (mm)	1	2	3	4	5
Computational time (s)	209.82	368.82	380.88	384.96	412.23

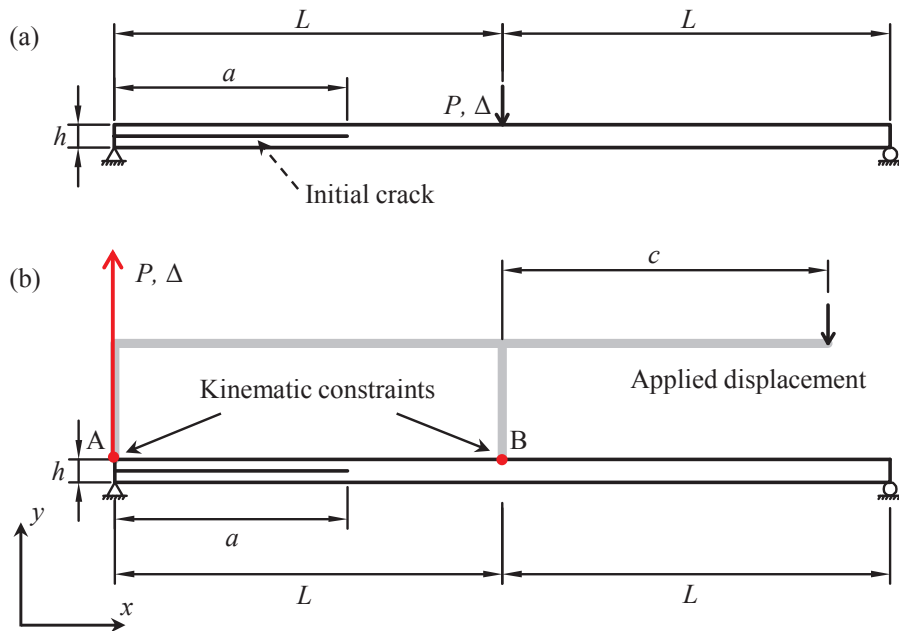


Fig. 16. Setup and loading conditions for: (a) ENF test; (b) MMB test.

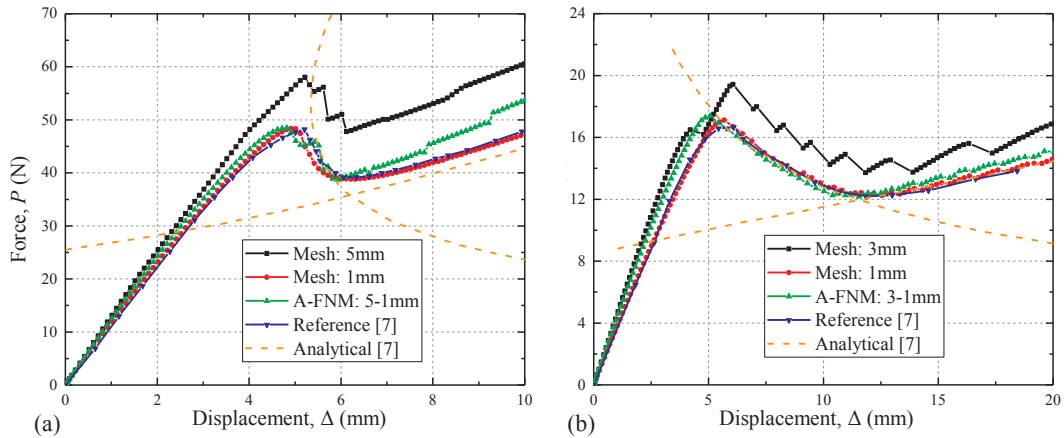


Fig. 17. Loading curves for: (a) ENF model; (b) MMB model.

Table 4
Computational time for ENF and MMB models (CPU time, X5690@3.47 GHz).

ENF	Mesh size (mm)	5	1	A-FNM 5-1
	Computational time (s)	23.2	29.09	24.47
MMB	Mesh size (mm)	3	1	A-FNM 3-1
	Computational time (s)	16.99	45.92	19.89

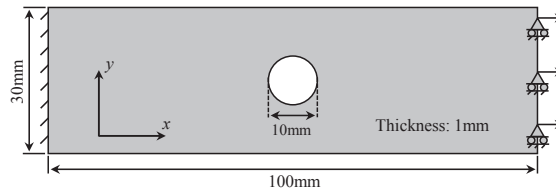


Fig. 18. OHT test: set-up and loading conditions.

The results of three modelling strategies are compared:

- FEM with global coarse 1 mm mesh (Fig. 12a);
- FEM with global refined 0.2 mm mesh (Fig. 12b) (Benchmark case);
- A-FNM with adaptive 1–0.2 mm mesh (Fig. 12c).

Here, “adaptive 1–0.2 mm mesh” means that outside the refined region, the size of elements is 1 mm (master and coarsened elements), while within the refinement zone, 0.2 mm sub elements are used.

The results obtained from both traditional FEM and the proposed A-FNM are presented in Figs. 13 and 14. The benchmark FEM model with 0.2 mm mesh provides accurate results, as expected. However, the globally 1 mm mesh is too coarse to correctly capture the onset and propagation of the delamination. On the other hand, applying the A-FNM to the coarse mesh results in acceptable accuracy: both the global load-displacement response and delamination propagation are correctly predicted. An additional case with adaptive 3–0.2 mm mesh also produced acceptable results; in this case, the initial mesh is 3 mm and 15 sub-CEs are allocated in the refined configurations to meet the 0.2 mm size requirement (i.e., $n_{CE} = 15$ in Fig. 3).

The computational cost for each modelling scheme is shown in Table 2. As can be expected, globally fine mesh is capable of accurate prediction but incurs a large computational time. In contrast, A-FNM results in saving of the computational time by up to 47%.

5.1.3. Sensitivity to refinement zone length

Next, the sensitivity of the A-FNM to the length of refinement zone is studied in Fig. 15.

As shown in Fig. 15, $l_{rf} = 1$ mm is not sufficient for accurate solution. l_{rf} equal to or larger than 2 mm are required but with increased computational cost (Table 3). With an appropriate choice of l_{rf} , estimated through Eq. (11), accurate and efficient modelling by A-FNM is possible.

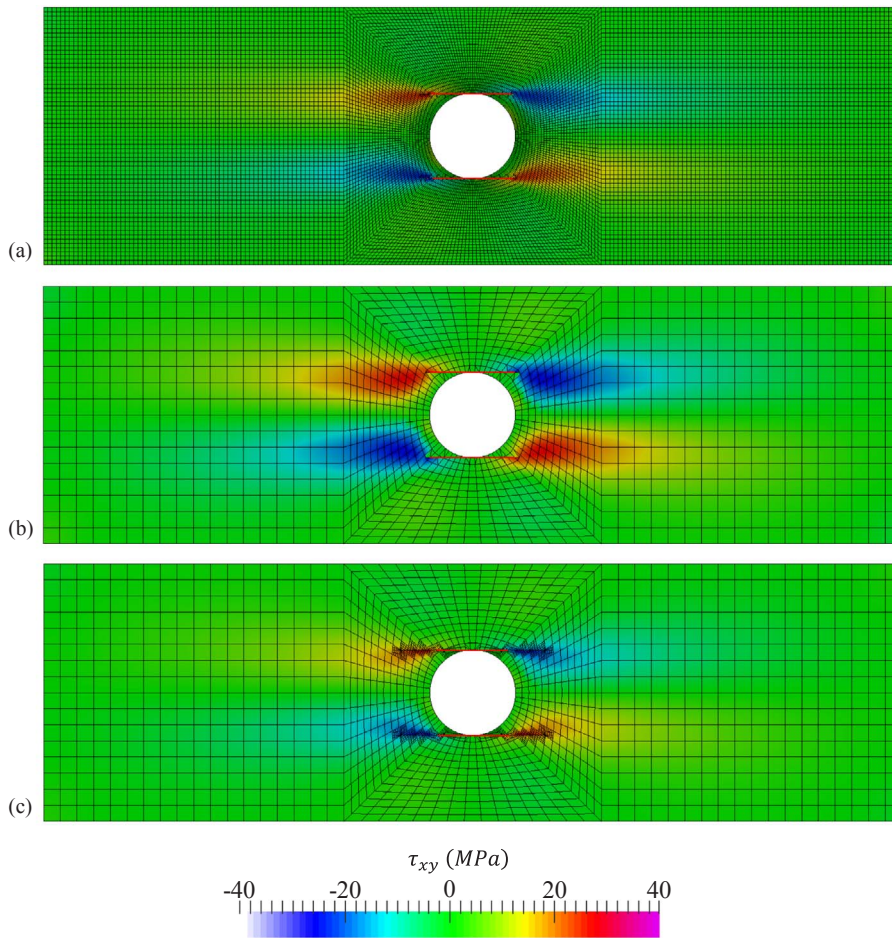


Fig. 19. Comparison between different models at initiation stage: (a) refined model; (b) coarse model; (c) A-FNM model.

5.2. End notch flexure (ENF) and mixed-mode bending (MMB) tests

The ENF (mode II) and MMB (mixed mode) tests in [7] are modelled in this subsection. Similar in-plane geometries as the DCB case are adopted for the ENF and MMB tests: length $2L = 100$ mm, thickness $h = 3$ mm, width 1 mm and initial crack length $a = 30$ mm (Fig. 16). For the MMB test, the prescribed displacement is applied at the right end of the rigid lever (with $c = 41.5$ mm). The material properties shown in Table 1 are used.

Since the mode II fracture toughness is higher than the mode I toughness, larger elements may be employed in the analysis based on the minimum size requirement predicted by Eq. (6). The force-displacement responses are compared with the reference and analytical results from [7] (Fig. 17). Models with coarse meshes tend to over predict the strength; however, by employing the A-FNM, the accuracy of the predictions is improved and close agreement with reference results is obtained.

Although the required computational time of ENF and MMB simulations is much less than the DCB test, time reduction is still expected with the A-FNM modelling. As shown in Table 4, employing the A-FNM, 16% and 57% time saving is achieved for the ENF and MMB tests, respectively.

5.3. Open-hole tension (OHT) of a unidirectional composite plate

The OHT of a unidirectional composite plate is analyzed here. The dimensions of the specimen are shown in Fig. 18, with the left edge constrained and a prescribed uniaxial displacement imposed on the right edge. All the plies are oriented at 0° , in the direction of the applied load. Again, material properties used in the model are given in Table 1.

Three structured meshes are used: 1. The benchmark is a very fine mesh with elements near the hole about 0.25 mm in size and those further from the hole about 0.5 mm (Fig. 19a); 2. Coarse mesh where the elements around the hole are about 1 mm and those away from the hole are about 2 mm (Fig. 19b); and 3. A-FNM with coarse initial mesh, with $n_{CE} \equiv 4$ in the refined region (Fig. 19c, for comparison with the fully refined model) and $l_{rf} \equiv 6$ mm based on material properties (Table 1).

The Tsai-Wu failure criterion is adopted to initiate the onset of matrix cracking [56] in the form of longitudinal splitting in the

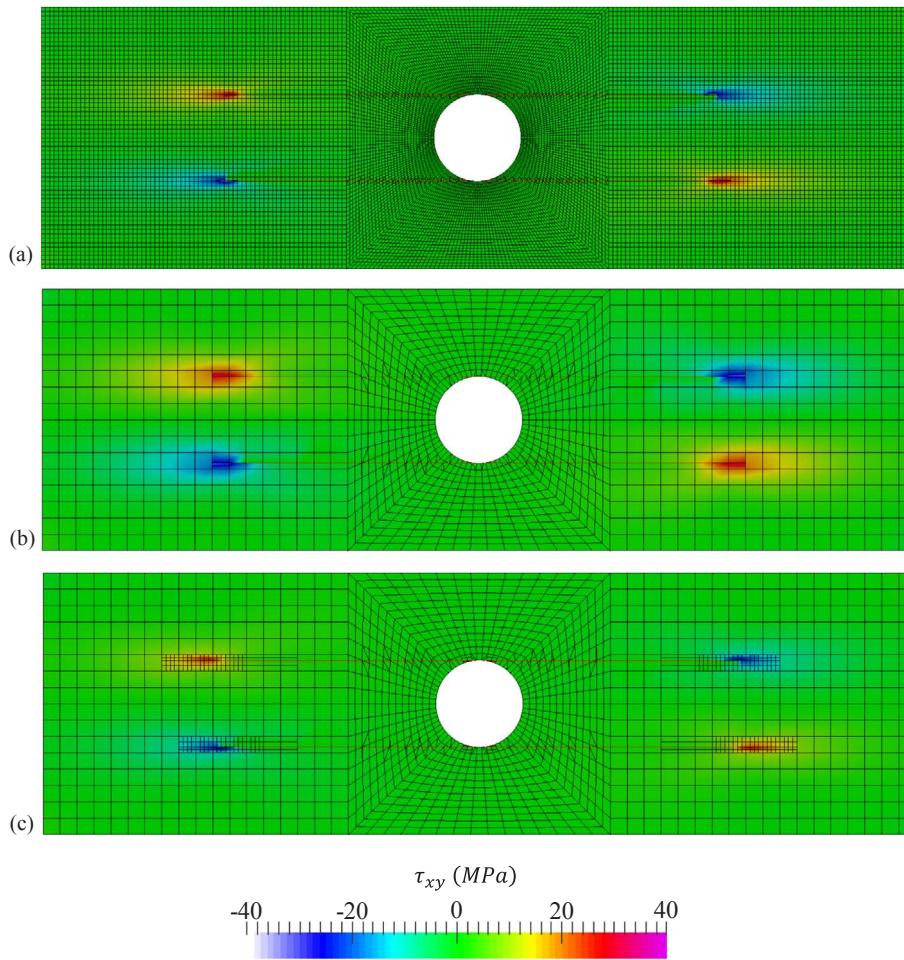


Fig. 20. Comparison between different models at propagation of longitudinal splits: (a) refined model; (b) coarse model; (c) A-FNM model.

fiber direction at hole edges (Fig. 19) driven by local shear stresses τ_{xy} . After initiation, the cracks continue to propagate along the fiber direction (Fig. 20), in agreement with experimental observations [57,58]. At both initiation and propagation stages, the coarse mesh model over predicts the high stress region around the crack fronts. However, with local refinement defined ahead of the crack tip, the A-FNM model provides stress distributions comparable to those given by the refined model. To further demonstrate the performance of the A-FNM, a random unstructured mesh is applied in the analysis. As shown in Fig. 21, similar observations are obtained and the stress profile is effectively captured in the moving refinement zone.

According to the loading responses obtained from both structured and unstructured meshes (Fig. 22), the A-FNM models correctly predict the splitting initiation as well as the subsequent damage process, which is in close agreement with the results of the benchmark refined models. However, the coarse mesh models significantly over-estimate the load at onset of splitting. As shown in Fig. 23, computational time saving of over 80% is achieved, if the proposed A-FNM is employed (81.4% and 82.5% for structured and unstructured meshes, respectively).

5.4. Delamination migration (DM) of cross-ply composite laminates

The proposed A-FNM is employed to model DM of cross-ply laminates [6,59]. The test setup is shown in Fig. 24a. Pre-crack is inserted in the specimen between the 0° and 90° plies and it may migrate to the upper interface through a matrix crack developed in the blocked 90° laminae. The layup and geometries adopted in the FE model is shown in Fig. 24b, and only the middle ply-block ([0/90/0₃/90₄/T/0/90₄]) is modelled by A-FNM elements. With clamping force $F_c = 1700$ N imposed at two ends and rigid contact (friction coefficient $\mu = 0.23$) defined between the specimen and the clamps, prescribed displacement is applied on the top surface of the specimen [6].

From the mesh refinement test, while models with 1 mm mesh over-predict the structural strength by about 100%, 0.2 mm mesh leads to converged results. In this case, models with globally fine 0.2 mm mesh are set as benchmarks and A-FNM is performed on the overall 1 mm mesh (with $n_{CE} \equiv 5$ and $l_{rf} \equiv 3$ mm). The comparisons between different models are given in the following.

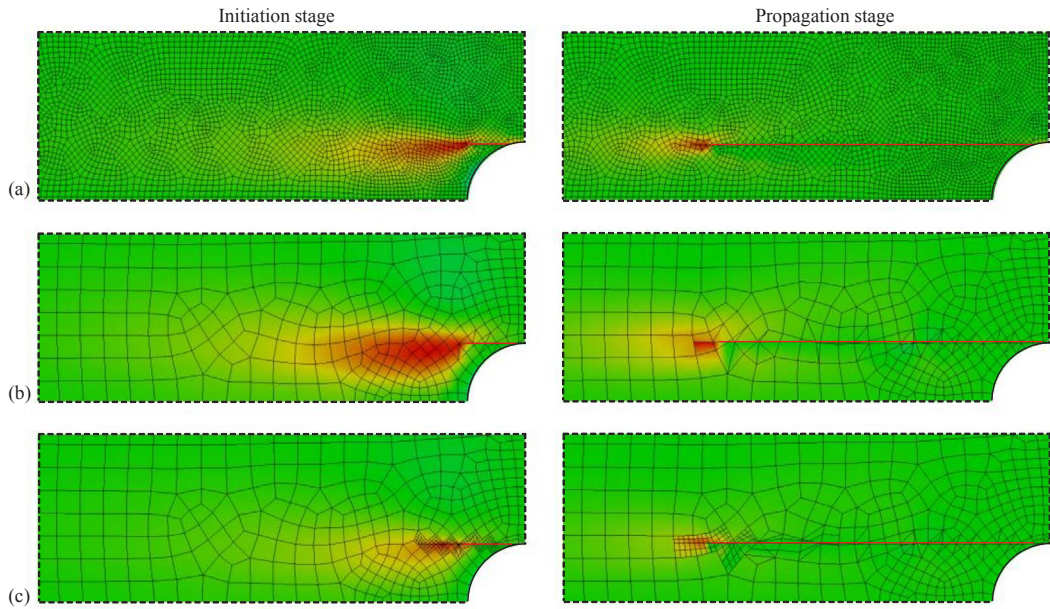


Fig. 21. Comparison between different models with unstructured meshes at initiation (left column) and propagation stages (right column): (a) refined model; (b) coarse model; (c) A-FNM model.

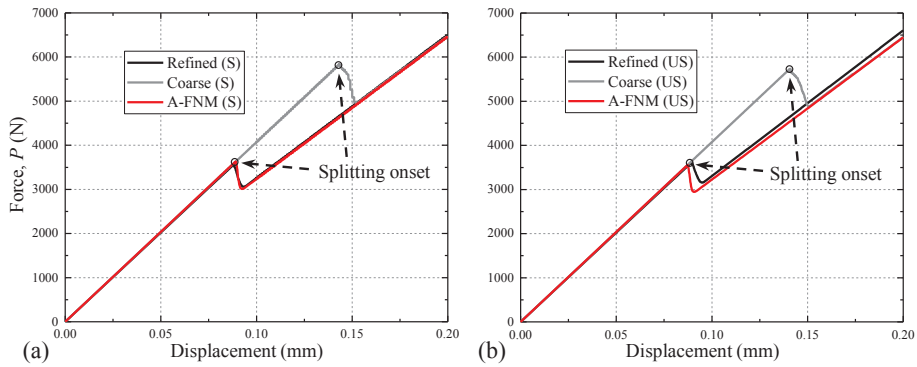


Fig. 22. Loading curves of different models with: (a) structured meshes (S); (b) unstructured meshes (US).

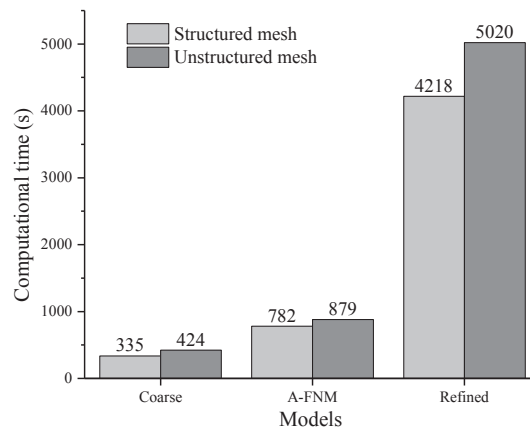


Fig. 23. OHT: computational time for different models (CPU time, X5690@3.47 GHz).

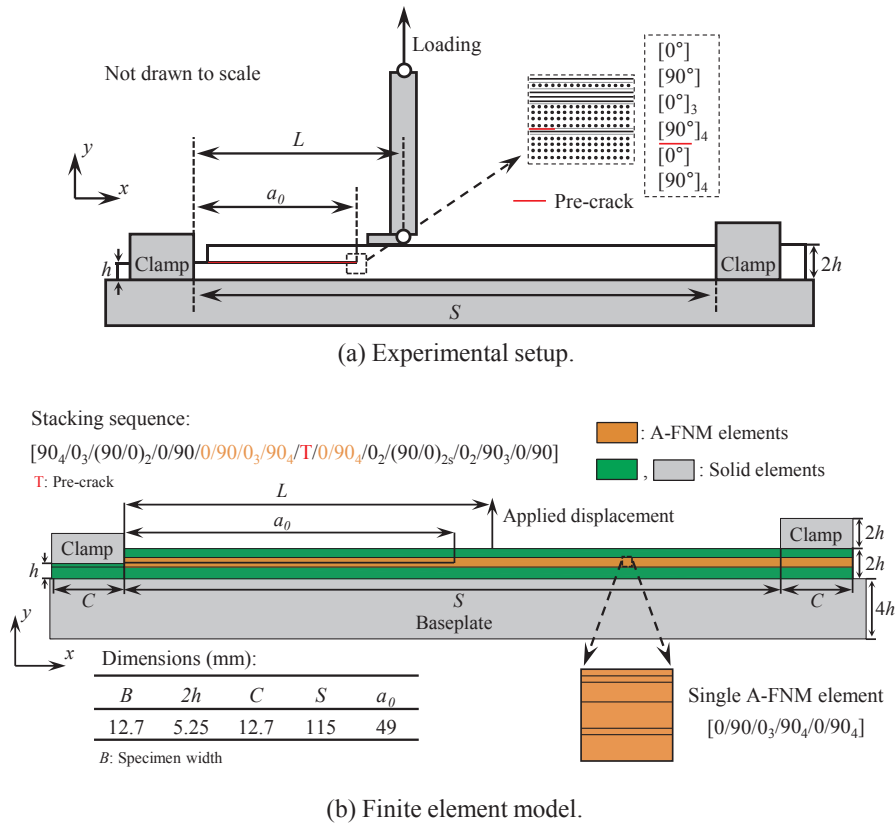


Fig. 24. Experimental setup [6,59] and finite element model for delamination migration test.

5.4.1. Loading responses and migration locations

With load offsets (L/a_0) ranging from 1.0 to 1.3, different load-displacement responses are obtained (Fig. 25). Although the models with 1 mm mesh fails to give correct predictions, the accuracy of modelling is substantially enhanced by applying the proposed A-FNM and consistent results are achieved compared to the benchmarks and experiments [6,59].

As has been reported in [6], similar failure events are observed in both fully refined and A-FNM models: after propagating at the lower interface for a certain distance, the delamination migrates and progresses along the upper interface. For the case $L = a_0$, unstable delamination is predicted to occur right after the maximum load, resulting in the first load-drop (Fig. 25a). However, when the delamination starts to migrate via crack kinking in the 90° plies, further loading is required to propagate the matrix crack, leading to the increase of the external load during the migration process. Once the delamination fully relocates onto the new interface, the second load-drop is experienced, representing unstable delamination growth along the upper interface. In general, the predicted failure events agree well with observations from experiments [6,59].

However, different damage sequences are observed for cases $L = 1.1a_0$ to $L = 1.3a_0$ (Fig. 25b–d). After the peak load, the stable delamination along the lower interface is firstly experienced, followed by unstable propagation once the crack front passes the loading position. The load-drop is expected, during which the migration occurs.

The predicted migration locations, Δ_M , further demonstrate the accuracy of the A-FNM modelling (Fig. 26). It is worth noting that all the migration locations predicted by the A-FNM models are within the experimental scatters.

5.4.2. Adaptive modelling and the efficiency

Fig. 27 shows the predicted failure patterns during the overall damage process. The local refinement moves with the advancing crack front, and after delamination migration, it relocates onto the new interface. It is shown in Fig. 27 that stress concentration ahead of the crack tip is accurately captured within the local refinement, thus ensuring the correctness of the damage prediction.

The computational cost for both fully refined and A-FNM models is given in Fig. 28. Compared to the fully refined models, about 74% of the computational time is saved if the A-FNM is adopted.

6. Conclusion

This paper presents a novel and efficient adaptive technique based on the floating node method for modelling coupled delamination and matrix cracking failure in laminated composite materials. The proposed adaptive floating node method (A-FNM) is able to

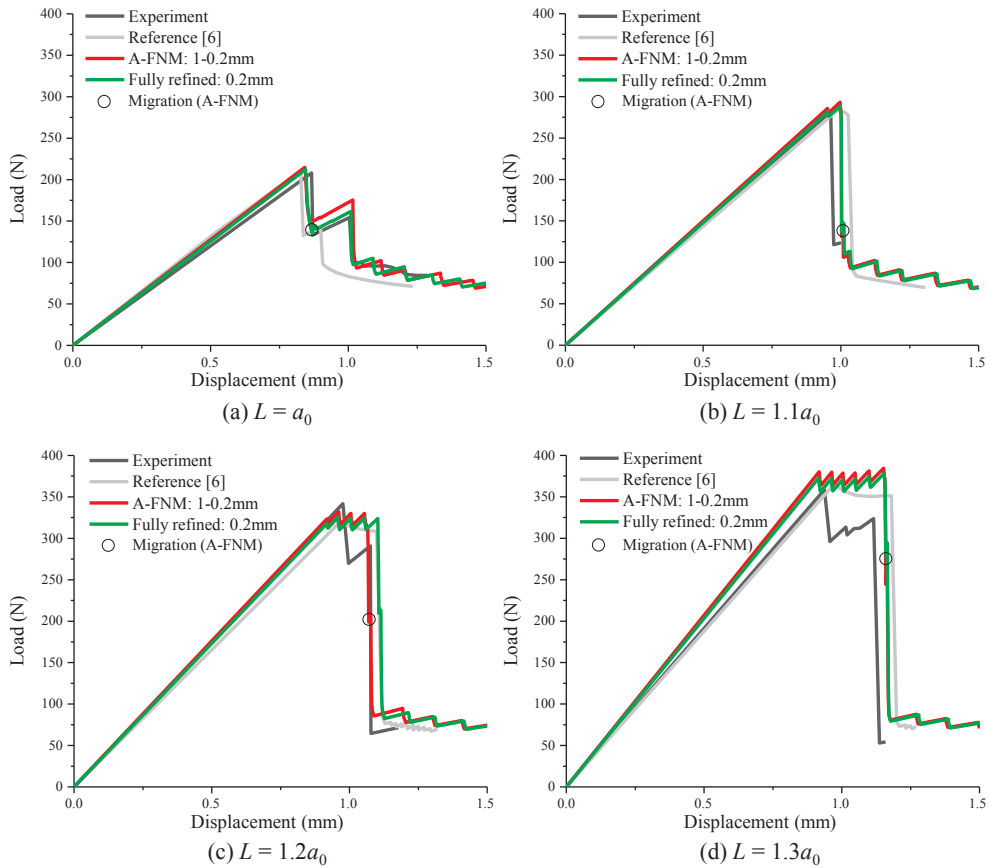


Fig. 25. Load-displacement curves for different load offsets: numerical predictions vs. experimental results [59].

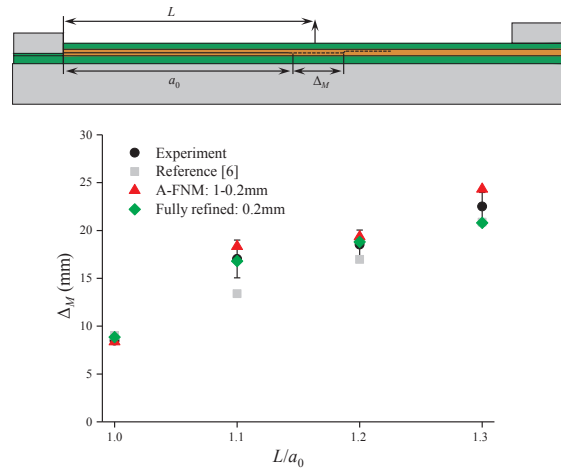


Fig. 26. Migration locations for different load offsets: numerical predictions vs. experimental results [59].

mitigate excessive mesh size requirements, thus significantly reducing computational cost.

The designed A-FNM element is capable of assuming several element configurations: the master element, refined element and coarsened element, depending on the propagation and proximity of the crack front. A refinement zone ahead of the crack tip is defined, wherein the elements should be sufficiently fine to accurately model composite failure process. When the crack front has propagated past the refinement zone, the mesh in the crack wake may be re-coarsened. An element coarsening criterion is proposed based on *a posteriori* error estimator for the element strain energy. In this way, refinement and re-coarsening can be performed efficiently.

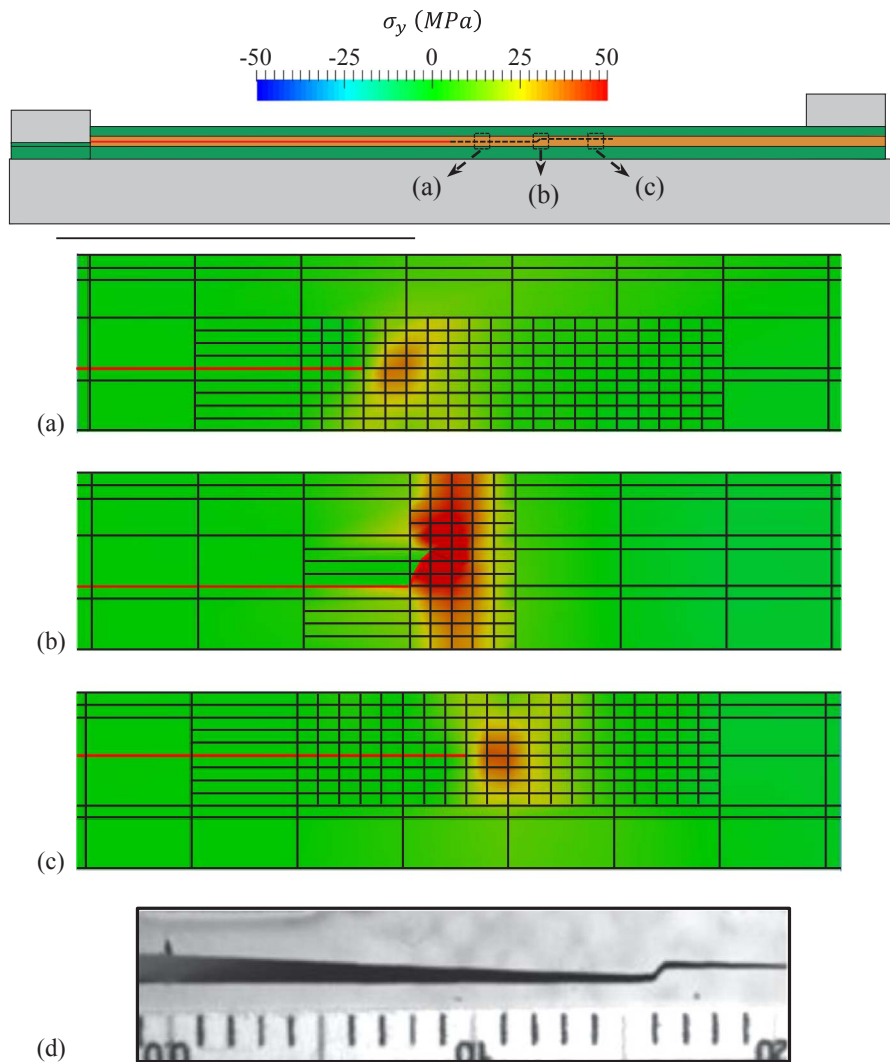


Fig. 27. A-FNM modelling of delamination migration: (a) delamination at the lower interface; (b) migration via matrix cracking; (c) delamination at the upper interface; (d) experimental record of migration [59].

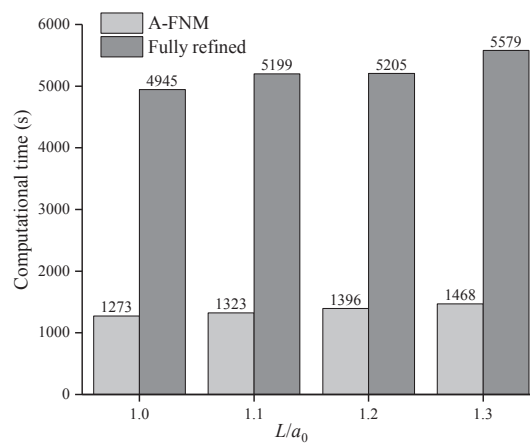


Fig. 28. Computational time for fully refined and A-FNM locally refined models (CPU time, X5690@3.47 GHz).

Several numerical examples, including mode I, mode II, mixed-mode delamination test, the OHT of unidirectional composite plate and delamination migration of cross-ply laminates, are provided to demonstrate the performance of A-FNM. The proposed A-FNM offers several advantages over the existing numerical techniques:

- The need for very fine global mesh is alleviated and up to 82.5% of computational time in the case of OHT can be saved.
- Reduction on materials strength is avoided [12], and therefore stress distribution ahead of the crack tip is accurately captured.
- Compared to adaptive mesh refinement (AMR) method [34,35], successive mesh regenerations and mesh information mapping are not required for A-FNM. Reductions in computational time and complexity of implementations can be achieved.

Acknowledgement

The first author greatly acknowledges the research scholarship and research grant (No. R265000523646) from National University of Singapore.

References

- [1] Tay TE. Characterization and analysis of delamination fracture in composites: an overview of developments from 1990 to 2001. *Appl Mech Rev* 2003;56:1–32.
- [2] Rybicki EF, Kanninen MF. A finite element calculation of stress intensity factors by a modified crack closure integral. *Engng Fract Mech* 1977;9:931–8.
- [3] Rybicki EF, Schmueser DW, Fox J. An energy release rate approach for stable crack growth in the free-edge delamination problem. *J Compos Mater* 1977;11:470–87.
- [4] Dugdale DS. Yielding of steel sheets containing slits. *J Mech Phys Solids* 1960;8:100–4.
- [5] Barenblatt GI. The mathematical theory of equilibrium cracks in brittle fracture. *Adv Appl Mech* 1962;7:55–129.
- [6] De Carvalho NV, Chen BY, Pinho ST, Ratcliffe JG, Baiz PM, Tay TE. Modeling delamination migration in cross-ply tape laminates. *Compos Part A Appl Sci Manuf* 2015;71:192–203.
- [7] Mi Y, Crisfield MA, Davies GAO, Hellweg HB. Progressive delamination using interface elements. *J Compos Mater* 1998;32:1246–72.
- [8] Alfano G, Crisfield MA. Finite element interface models for the delamination analysis of laminated composites: mechanical and computational issues. *Int J Numer Meth Engng* 2001;50:1701–36.
- [9] Remmers JJC, Borst Rd, Needleman A. A cohesive segments method for the simulation of crack growth. *Comput Mech* 2003;31:69–77.
- [10] Camanho PP, Davila CG, De Moura MF. Numerical simulation of mixed-mode progressive delamination in composite materials. *J Compos Mater* 2003;37:1415–38.
- [11] Borst Rd, Remmers JJC, Needleman A. Mesh-independent discrete numerical representations of cohesive-zone models. *Engng Fract Mech* 2006;73:160–77.
- [12] Turon A, Davila CG, Camanho PP, Costa J. An engineering solution for mesh size effects in the simulation of delamination using cohesive zone models. *Engng Fract Mech* 2007;74:1665–82.
- [13] Sarrado C, Turon A, Renart J, Urresti I. Assessment of energy dissipation during mixed-mode delamination growth using cohesive zone models. *Compos Part A Appl Sci Manuf* 2012;43:2128–36.
- [14] Hosseini S, Remmers JJC, Verhoosel CV, Borst Rd. Propagation of delamination in composite materials with isogeometric continuum shell elements. *Int J Numer Meth Engng* 2015;102:159–79.
- [15] Higuchi R, Okabe T, Yoshimura A, Tay TE. Progressive failure under high-velocity impact on composite laminates: experiment and phenomenological meso-modeling. *Engng Fract Mech* 2017;178:346–61.
- [16] Areias PMA, Song JH, Belytschko T. Analysis of fracture in thin shells by overlapping paired elements. *Comput Methods Appl Mech Eng* 2006;195:5343–60.
- [17] Zhao LB, Zhi J, Zhang JY, Liu ZL, Hu N. XFEM simulation of delamination in composite laminates. *Compos Part A Appl Sci Manuf* 2016;80:61–71.
- [18] Hu XF, Chen BY, Tirvaudey M, Tan VBC, Tay TE. Integrated XFEM-CE analysis of delamination migration in multi-directional composite laminates. *Compos Part A Appl Sci Manuf* 2016;90:161–73.
- [19] Chen BY, Pinho ST, De Carvalho NV, Baiz PM, Tay TE. A floating node method for the modelling of discontinuities in composites. *Engng Fract Mech* 2014;127:104–34.
- [20] Chen BY, Tay TE, Pinho ST, Tan VBC. Modelling the tensile failure of composites with the floating node method. *Comput Methods Appl Mech Eng* 2016;308:414–42.
- [21] Chen BY, Tay TE, Pinho ST, Tan VBC. Modelling delamination migration in angle-ply laminates. *Compos Sci Technol* 2017;142:145–55.
- [22] Iarve EV, Gurvich MR, Mollenhauer DH, Rose CA, Dávila CG. Mesh-independent matrix cracking and delamination modeling in laminated composites. *Int J Numer Meth Engng* 2011;88:749–73.
- [23] Mollenhauer D, Ward L, Iarve E, Putthanasarat S, Hoos K, Hallett S, et al. Simulation of discrete damage in composite overheight compact tension specimens. *Compos Part A Appl Sci Manuf* 2012;43:1667–79.
- [24] Hoos K, Iarve EV, Braginsky M, Zhou E, Mollenhauer DH. Static strength prediction in laminated composites by using discrete damage modeling. *J Compos Mater* 2016;51:1473–92.
- [25] Higuchi R, Okabe T, Nagashima T. Numerical simulation of progressive damage and failure in composite laminates using XFEM/CZM coupled approach. *Compos Part A Appl Sci Manuf* 2017;95:197–207.
- [26] Harper PW, Hallett SR. Cohesive zone length in numerical simulations of composite delamination. *Engng Fract Mech* 2008;75:4774–92.
- [27] Soto A, González EV, Maimí P, Turon A, de Aja JRS, de la Escalera FM. Cohesive zone length of orthotropic materials undergoing delamination. *Engng Fract Mech* 2016;159:174–88.
- [28] Guíamatsia I, Ankersen JK, Davies GAO, Iannucci L. Decohesion finite element with enriched basis functions for delamination. *Compos Sci Technol* 2009;69:2616–24.
- [29] Guíamatsia I, Davies GAO, Ankersen JK, Iannucci L. A framework for cohesive element enrichment. *Compos Struct* 2010;92:454–9.
- [30] Guíamatsia I, Ankersen JK, Iannucci L, Fouinneteau M. Enriched finite elements for the efficient prediction of impact-induced damage in composite laminates. *Compos Sci Technol* 2013;79:87–96.
- [31] Babuška I, Rheinboldt WC. A-posteriori error estimates for the finite element method. *Int J Numer Meth Engng* 1978;12:1597–615.
- [32] Zienkiewicz OC, Zhu JZ. A simple error estimator and adaptive procedure for practical engineering analysis. *Int J Numer Meth Engng* 1987;24:337–57.
- [33] Ainsworth M, Oden JT. A posteriori error estimation in finite element analysis. *Comput Methods Appl Mech Eng* 1997;142:1–88.
- [34] Park K, Paulino GH, Celes W, Espinha R. Adaptive mesh refinement and coarsening for cohesive zone modeling of dynamic fracture. *Int J Numer Meth Engng* 2012;92:1–35.
- [35] Kim J, Simone A, Duarte CA. Mesh refinement strategies without mapping of non-linear solutions for the generalized and standard FEM analysis of 3-D cohesive fractures. *Int J Numer Meth Engng*; 2016.
- [36] Khoei AR, Moslemi H, Ardakany KM, Barani OR, Azadi H. Modeling of cohesive crack growth using an adaptive mesh refinement via the modified-SPR technique. *Int J Fracture* 2009;159:21–41.
- [37] Khoei AR, Eghbalian M, Moslemi H, Azadi H. Crack growth modeling via 3D automatic adaptive mesh refinement based on modified-SPR technique. *Appl Math*

- Model 2013;37:357–83.
- [38] Moslemi H, Khoei AR. 3D adaptive finite element modeling of non-planar curved crack growth using the weighted superconvergent patch recovery method. *Engng Fract Mech* 2009;76:1703–28.
- [39] Shor O, Vaziri R. Adaptive insertion of cohesive elements for simulation of delamination in laminated composite materials. *Engng Fract Mech* 2015;146:121–38.
- [40] Samimi M, Van Dommelen JAW, Geers MGD. A three-dimensional self-adaptive cohesive zone model for interfacial delamination. *Comput Methods Appl Mech Eng* 2011;200:3540–53.
- [41] Främby J, Fagerström M, Brouzoulis J. Adaptive modelling of delamination initiation and propagation using an equivalent single-layer shell approach. *Int J Numer Meth Engng* 2017;112:882–908.
- [42] Chen L, Lingen FJ, Borst Rd. Adaptive hierarchical refinement of NURBS in cohesive fracture analysis. *Int J Numer Meth Engng* 2017.
- [43] Brouzoulis J, Fagerström M, Svenning E. An enriched shell element formulation for modeling of inter- and intralaminar crack propagation in laminates. *Compos Struct* 2016;136:616–25.
- [44] Främby J, Brouzoulis J, Fagerström M. Assessment of two methods for the accurate prediction of transverse stress distributions in laminates. *Compos Struct* 2016;140:602–11.
- [45] Park K, Paulino GH. Cohesive zone models: a critical review of traction-separation relationships across fracture surfaces. *Appl Mech Rev* 2011;64:060802.
- [46] Hillerborg A, Modéer M, Petersson PE. Analysis of crack formation and crack growth in concrete by means of fracture mechanics and finite elements. *Cem Concr Res* 1976;6:773–81.
- [47] Suo Z. Remarks on crack-brfdgng concepts. *Appl Mech Rev* 1992;45:355.
- [48] Cox BN, Marshall DB. Concepts for bridged cracks in fracture and fatigue. *Acta Metall Mater* 1994;42:341–63.
- [49] Sih GC, Paris PC, Irwin GR. On cracks in rectilinearly anisotropic bodies. *Int J Fracture* 1965;1:189–203.
- [50] Cox BN, Lo CS. Simple approximations for bridged cracks in fibrous composites. *Acta Metall Mater* 1992;40:1487–96.
- [51] Yang QD, Cox BN, Nalla RK, Ritchie RO. Fracture length scales in human cortical bone: the necessity of nonlinear fracture models. *Biomaterials* 2006;27:2095–113.
- [52] Yang QD, Cox BN. Cohesive models for damage evolution in laminated composites. *Int J Fracture* 2005;133:107–37.
- [53] Falk ML, Needleman A, Rice JR. A critical evaluation of cohesive zone models of dynamic fracture. *J Phys IV* 2001;11:543–50.
- [54] Benzeggagh ML, Kenane M. Measurement of mixed-mode delamination fracture toughness of unidirectional glass/epoxy composites with mixed-mode bending apparatus. *Compos Sci Technol* 1996;56:439–49.
- [55] Reeder JR, Demarco K, Whitley KS. The use of doubler reinforcement in delamination toughness testing. *Compos Part A Appl Sci Manuf* 2004;35:1337–44.
- [56] Tsai SW, Wu EM. A general theory of strength for anisotropic materials. *J Compos Mater* 1971;5:58–80.
- [57] Daken HH, Mar JW. Splitting initiation and propagation in notched unidirectional graphite/epoxy composites under tension-tension cyclic loading. *Compos Struct* 1985;4:111–33.
- [58] Green BG, Wisnom MR, Hallett SR. An experimental investigation into the tensile strength scaling of notched composites. *Compos Part A Appl Sci Manuf* 2007;38:867–78.
- [59] Ratcliffe JG, Czabaj MW, O'Brien TK. A test for characterizing delamination migration in carbon/epoxy tape laminates; 2013.